GAFD Special issue on "Physics and Algorithms of the Pencil Code"

Non-Fourier description of heat flux evolution in 3D MHD simulations of the solar corona

Jörn Warnecke†* and Sven Bingert‡

†Max Planck Institute for Solar System Research, Justus-von-Liebig-Weg 3, D-37077 Göttingen, Germany
‡Gesellschaft für wissenschaftliche Datenverarbeitung mbH Göttingen, Am Faßberg 11, 37077 Göttingen

(*November 5, 2018*)

The hot loop structures in the solar corona can be well modeled by three dimensional magnetohydrodynamic simulations, where the corona is heated by field line braiding driven at the photosphere. To be able to reproduced the emission comparable to observations, one has to use realistic values for the Spitzer heat conductivity, which puts a large constrain on the time step of these simulations and therefore make them computationally expensive. Here, we present a non-Fourier description of the heat flux evolution, which allow us to speed up the simulations significantly. Together with the semi-relativistic Boris correction, we are able to limit the time step constrain of the Alfvén speed and speed up the simulations even further. We discuss the implementation of these two methods to the Pencil Code and present their implications on the time step, and the temperature structures, the ohmic heating rate and the emission in simulations of the solar corona. We find that with the use of the non-Fourier description of the heat flux evolution and the Boris correction, we can increase the time step of the simulation significantly without moving far away from the reference solution. However, for too low values of the Alfvén speed limit, the simulation moves away from the reference solution und produces much higher temperatures and stronger emission structures.

Keywords: magnetohydrodynamics, solar corona, Sun, magnetic fields, coronal heating

1. Introduction

The solar corona can be characterized by a plasma at low densities and high temperatures. With the presence of coronal magnetic fields, this leads to low β plasma, i.e. the magnetic pressure is higher than the gas pressure. Therefore, the plasma motions are dominated by the magnetic field, so the plasma can organize itself in closed loop structures. The corona emits radiation in extreme UV and X-ray emission, making it observable from space-based telescopes. One of the major open questions concerning the solar corona is its heating mechanism, i.e. why is the solar corona typically more than 100 times hotter than the photosphere. One of the ideas of explaining coronal heating is the field-line braiding model by Parker (1972, 1988), in which magnetic energy is released in form of nanoflares. In this model the magnetic footpoints of the loops are irreversible moved by the small-scale photospheric motions, get braided in chromosphere and corona, where the reconnecting field lines release magnetic energy in terms of ohmic heating to the thermal energy budget. Three dimensional magnetohydrodynamic simulations modeling the solar corona were able to show that with this nanoflare heating mechanism the basic temperature structure and its dynamics can be reproduced (e.g. Gudiksen and Nordlund 2002, 2005b, Bingert and Peter 2011). These models are able to describe energy transport to

---

*Corresponding author. Email: warnecke@mps.mpg.de

the corona consistent with the nanoflare model (Bingert and Peter 2013). This type of simulations are further used to synthesize coronal emission and compare the actual observation of the corona. From these synthesized emission, one finds that these models are able to reproduce the average Doppler shifts (Peter *et al.* 2004, 2006, Hansteen *et al.* 2010) and the formation of coronal loops, when using a data driven model with an observed photospheric magnetic field (Bourdin *et al.* 2013, 2014). These models were used to show that the coronal magnetic field structure is close to a potential field (Gudiksen and Nordlund 2005b, Bingert and Peter 2011), and therefore close to force-free. However, the force-free approximation, broadly used to obtain coronal magnetic field with field extrapolations (for a review, we refer to Wiegelmann 2008), turns out to be not always valid (Peter *et al.* 2015) and fails to described complex current structures in coronal loops above emerging active regions (Warnecke *et al.* 2017). Recently, Rempel (2017) showed that the solar corona can be heated by a small-scale dynamo operating in the near-surface region of convection zone braiding the magnetic footpoints in the photosphere. Therefore, these types of models are able to reproduce the main properties of the solar corona on the resolved scale (e.g. Peter 2015). One of the most important ingredient is the vertical Poynting flux at the bottom of the corona. Furthermore, the numerical models need to use a Spitzer heat flux which is dominantly aligned with the magnetic field, using a realistic value of the Spitzer heat conductivity to be able to reproduce the coronal emissions correctly, i.e. comparable to observations.

Currently there are only a limited number of codes available which are used for this kind of simulations. One of the most used codes to simulated the solar corona is the BIFROST code (Gudiksen *et al.* 2011), which is based on earlier work of Gudiksen and Nordlund (2002, 2005b,a) and the STAGGER code (Galsgaard and Nordlund 1996). In these simulations, the near-surface convection is included, which drive the photospheric velocities self-consistently. Furthermore, the BIFROST code include a realistic treatment of the chromosphere using non-local thermal equilibrium. Another code is the MURAM code (Vögler *et al.* 2005, Rempel 2014), that has been recently extended to the upper atmosphere (Rempel 2017). Also, there, the photospheric motions are driven by near-surface convection and currently the chromosphere is treated as local thermal equilibrium. Apart of these codes there are other codes used for realistic modeling of the solar corona (e.g. Abbett 2007, Mok *et al.* 2005, 2008, van der Holst *et al.* 2014).

In this paper, we present an extension to the coronal model of the PENCIL CODE[1], that has been used to successfully described the solar corona using either observed magnetograms and velocity driver mimicking the photospheric motions (Bingert and Peter 2011, 2013, Bourdin *et al.* 2013) or flux emergence simulations (Chen *et al.* 2014, 2015) as input at the lower boundary instead of simulating near-surface convection. However, Chatterjee (2018) developed a 2D model, where the near-surface convection is included with a realistic treatment of the solar corona. Simplified two-layer simulations of the convection zone and the corona of the Sun and stars using the PENCIL CODE have been successfully used to investigate the dynamo-corona interplay (Warnecke and Brandenburg 2014, Warnecke *et al.* 2016a), to self-consistently drive current helicity ejection into the corona (Warnecke and Brandenburg 2010, Warnecke *et al.* 2011, 2012a, 2013a) and the formation of sunspot-like flux concentrations (Warnecke *et al.* 2013b, 2016b, Losada *et al.* 2018).

To be able to compare the simulations of the solar corona with observations of emissivities, one need to use a realistic value of Spitzer heat conductivity. However, this put a major constraint on the time step in these simulation. For simulation with a grid spacing of around 200 km the time step due to the Spitzer heat conductivity is around 1 ms. If one want to study the dynamics on smaller scales and being able to reduce the fluid and magnetic diffusivities, one needs to use higher resolution. The smaller grid spacing leads

---

[1]http://github.com/pencil-code

to even lower values of the time steps. As the time step decreased quadratically with grid spacing, the simulations become unfeasible for very high resolutions. To circumvent this, Chen *et al.* (2014), for example, used a sub-stepping scheme and Rempel (2017) used a non-Fourier scheme, where the hyperbolic equation for the heat transport is solved. Similar approaches have also been used in the dynamo community to describe non-local evolution of the turbulent electromagnetic force (Brandenburg *et al.* 2004, Hubbard and Brandenburg 2009, Rheinhardt and Brandenburg 2012, Brandenburg and Chatterjee 2018). We present here a non-Fourier description of the Spitzer heat flux, which have been recently implemented to the PENCIL CODE, see Section 2.2. We compare the outcome of the simulations obtained with and without the non-Fourier scheme, see Section 3. Furthermore, we also compare these simulations to those using the semi-relativistic Boris correction (Boris 1970) to the Lorentz force, which have been also recently implemented to the PENCIL CODE (Chatterjee 2018) to limit the time step constrains due to the Alfvén speed, see Section 2.3.

2. Setup

The setup of the simulations is based on the model of Bingert and Peter (2011, 2013), therefore a detailed description will not be repeated here. We model a part of the solar corona in a Cartesian box (x,y,z) of $100 \times 100 \times 60$ Mm^3. The $z = 0$ layer represent the solar photosphere. We use $128 \times 128 \times 256$ grid points, corresponding to a resolution of 781 km in the horizontal 234 km in the vertical direction. We solve the compressible magnetohydrodynamic equations for the density ρ, the velocity $\boldsymbol{u}$, the magnetic vector potential $\boldsymbol{A}$ and the temperature T.

$$\frac{\mathrm{D} \ln \rho}{\mathrm{D} t} = -\boldsymbol{\nabla} \cdot \boldsymbol{u}, \tag{1}$$

$$\frac{\mathrm{D} \boldsymbol{u}}{\mathrm{D} t} = -\frac{\boldsymbol{\nabla} p}{\rho} + \boldsymbol{g} + \frac{\boldsymbol{J} \times \boldsymbol{B}}{\rho} + \frac{1}{\rho} \boldsymbol{\nabla} \cdot 2\nu\rho\mathbf{S}, \tag{2}$$

$$\frac{\mathrm{D} \ln T}{\mathrm{D} t} + (\gamma - 1) \boldsymbol{\nabla} \cdot \boldsymbol{u} = \frac{1}{c_\mathrm{V} \rho T} \left[\mu_0 \eta \boldsymbol{J}^2 + 2\rho\nu\mathbf{S}^2 + \boldsymbol{\nabla} \cdot \boldsymbol{q} + L \right] \tag{3}$$

where we use a constant gravity $\boldsymbol{g} = (0, 0, -g)$ with $g = 274 \, \mathrm{m/s}^2$, a rate of strain tensor $\mathbf{S} = 1/2(u_{i,j} + u_{j,i}) - 1/3\delta_{ij}\boldsymbol{\nabla} \cdot \boldsymbol{u}$ and a constant viscosity ν throughout the domain. Additional we use a shock viscosity to resolve shocks formed by high Mach number flows; see Haugen *et al.* (2004) and Gent *et al.* (2013) for details regarding its implementation. The pressure $p = \frac{k_\mathrm{B}}{\mu \, m_\mathrm{p}} \rho T$ is given by the equation of state of an ideal gas, where k_B, μ and m_p are Boltzmann constant, the molecular weight and the proton mass, respectively. The corresponding adiabatic index $\gamma = c_\mathrm{P}/c_\mathrm{V}$ is $5/2$, with the specific heats at constant pressure c_P and constant volume c_V. The heat flux $\boldsymbol{q}$ is given by anisotropic Spitzer heat conduction

$$\boldsymbol{q} = K_0 \left(\frac{T}{[K]} \right)^{5/2} \frac{\boldsymbol{B}\boldsymbol{B}}{\boldsymbol{B}^2} \boldsymbol{\nabla} T \equiv \boldsymbol{\mathcal{K}} \boldsymbol{\nabla} T, \tag{4}$$

which only give a contribution aligned with the magnetic field and $K_0 = 2 \times 10^{-11}\,\mathrm{W(mK)}^{-1}$ is the Spitzer value. For some of the runs we replaced this equation by the hyperbolic equation of the non-Fourier heat flux, see Section 2.2. Because of numerical stability, additionally to the anisotropic Spitzer heat conduction, we apply an isotropic heat conduction, which is proposal to $|\boldsymbol{\nabla} \ln T|$ and a heat conduction with a constant heat diffusivity $\chi = K/c_\mathrm{P}\rho$. The radiative losses due to the optically thin part of the atmosphere are described by $L = -n_\mathrm{e}n_\mathrm{H}Q(T)$, where n_e and n_H are the electron and hydrogen particle densities. $Q(T)$ describes the radiative losses as a function of temperature following the model of Cook *et al.* (1989); for details see Bingert (2009).
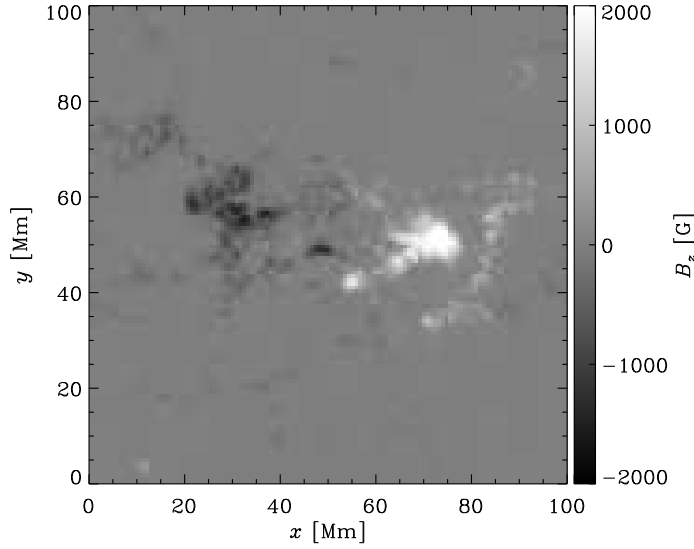
Jörn Warnecke and Sven Bingert

Figure 1. Initial vertical magnetic field B_z at the photospheric layer $z = 0$.

To full-fill exact solenoidality for the magnetic field $\boldsymbol{B} = \boldsymbol{\nabla} \times \boldsymbol{A}$ at all times, we solve for the induction equation for Vector potential $\boldsymbol{A}$.

$$\frac{\partial \boldsymbol{A}}{\partial t} = \boldsymbol{u} \times \boldsymbol{B} + \eta \boldsymbol{\nabla}^2 \boldsymbol{A}, \tag{5}$$

where we use the resistive gauge. The current is given by $\boldsymbol{J} = \boldsymbol{\nabla} \times \boldsymbol{B}$ and η is the magnetic diffusivity.

2.1. *Initial and boundary conditions*

At the lower boundary we use the vertical magnetic field of the line-of-site magnetic field from the active region AR 11102, observed on the 30th of August with the Helioseismic and Magnetic Imager (HMI; Schou *et al.* 2012) onboard of the Solar Dynamics Observatory (SDO), see Fig. 1 for an illustration. As an initial condition, we use a potential field extrapolation to fill the whole box with magnetic fields. For the temperature, we use an initial profile of a simplified representation of the solar atmosphere, similar as in Bingert and Peter (2011). The density is calculated accordingly using hydrostatic equilibrium. The velocities are initially set to zero.

The simulations are driven by a prescribed horizontal velocity field at the lower boundary mimicking the pattern of surface convection. As discussed in Gudiksen and Nordlund (2002, 2005b), Bingert (2009), Bingert and Peter (2011), such a surface velocity driver is able to reproduce the observed photospheric velocity spectrum in space and time. To avoid the destruction of the magnetic field pattern caused by the photospheric velocities, we apply the following to stabilize the field: i) we lower the magnetic diffusivity in the two lowest grid layers, ii) we apply a quenching of velocities, when magnetic pressure is larger than the gas pressure and iii) we interpolate between the current vertical magnetic field and the initial one B_z^{int} at $z = 0$ layer following

$$\frac{\partial B_z}{\partial t} = \frac{1}{\tau_b} \left(B_z^{\text{int}} - B_z \right), \tag{6}$$

where $\tau_b = 10\,\text{mins}$ is the relaxation time. We apply a potential field boundary condition at the bottom and top boundary of box for the magnetic field. The temperature and density are kept fix at the bottom boundary. At the top boundary, we set the velocities to zero to prevent

mass leaving or entering the simulation, also the heat flux is set to zero at the boundary. All quantities are periodic in horizontal directions.

For the viscosity and magnetic diffusivity we choose $\nu = 10^{10}\,\mathrm{m^2/s}$ and $\eta = 2 \times 10^{10}\,\mathrm{m^2}/s$.

2.2. *Non-Fourier heat flux scheme*

To reduce the time step constrains due to the Spitzer heat conductivity, we use a non-Fourier description and solve for the heat flux $\boldsymbol{q}$

$$\frac{\partial \boldsymbol{q}}{\partial t} = -\frac{1}{\tau_{\mathrm{Spitzer}}}\left(\boldsymbol{q} - \boldsymbol{\mathcal{K}}\boldsymbol{\nabla}T\right), \tag{7}$$

where τ_{Spitzer} is the heat flux relaxation time, i.e. e-folding time for $\boldsymbol{q}$ to approach $\boldsymbol{\mathcal{K}}\boldsymbol{\nabla}T$. $\boldsymbol{\mathcal{K}}$ is the Spitzer heat conductivity tensor, which has contribution only along the magnetic field. This approach enables us to use a different time stepping constrain to solve our equation. Instead of using the time step of Spitzer heat conduction $\mathrm{d}t_{\mathrm{Spitzer}} = \mathrm{d}x^2/\chi_{\mathrm{Spitzer}}$ with $\chi_{\mathrm{Spitzer}} = |\boldsymbol{\mathcal{K}}|/\rho c_{\mathrm{V}}$ and $\mathrm{d}x$ being the grid spacing, we find two new time step constrains

$$\mathrm{d}t_1 = \mathrm{d}x\sqrt{\left(\frac{\tau_{\mathrm{Spitz}}}{\chi_{\mathrm{Spitzer}}}\right)} \equiv \frac{\mathrm{d}x}{c_{\mathrm{Spitz}}},\text{and} \quad \mathrm{d}t_2 = \tau_{\mathrm{Spitzer}}, \tag{8}$$

where $\mathrm{d}t_1$ comes from the wave propagation speed c_{Spitzer}, because Equation (7) can be rewritten as a waves equation. By certain choices of τ_{Spitzer}, we can significantly increase the time step. Furthermore, because $\mathrm{d}t_1$ depends linear on the grid spacing $\mathrm{d}x$, instead of quadric as $\mathrm{d}t_{\mathrm{Spitzer}}$, the ratio $\mathrm{d}t_1/\mathrm{d}t_{\mathrm{Spitzer}}$ i.e. the speed up grows for higher resolution, which leads to a computational gain. Both time step constrains are include in the CFL condition to calculate the time step of the simulation.

The major part of the heat flux is concentrated in the transition region, where the temperature gradient is high. This can lead to strong gradients in the heat flux $\boldsymbol{q}$ itself. We, therefore, normalize $\boldsymbol{q}$ by the density ρ to decrease the heat flux in the lower part of the transition region compared to the upper part. This results in a new set of equations.

$$\tilde{\boldsymbol{q}} = \frac{\boldsymbol{q}}{\rho} \tag{9}$$

We basically solve now for the energy flux per unit particle instead of the energy flux density.

$$\frac{\partial \tilde{\boldsymbol{q}}}{\partial t} = \frac{1}{\rho}\frac{\partial \boldsymbol{q}}{\partial t} + \boldsymbol{q}\frac{\partial \ln \rho}{\partial t} = -\frac{1}{\tau_{\mathrm{Spitzer}}}\left(\tilde{\boldsymbol{q}} - \frac{\boldsymbol{\mathcal{K}}}{\rho}\boldsymbol{\nabla}T\right) + \tilde{\boldsymbol{q}}\left(\boldsymbol{u}\cdot\boldsymbol{\nabla}\ln\rho + \boldsymbol{\nabla}\cdot\boldsymbol{u}\right), \tag{10}$$

where we use the continue equation for the last term. The term in the energy equation changes also correspondingly

$$\frac{\partial \ln T}{\partial t} = -\frac{1}{Tc_{\mathrm{V}}}\left(\boldsymbol{\nabla}\cdot\tilde{\boldsymbol{q}} + \tilde{\boldsymbol{q}}\cdot\boldsymbol{\nabla}\ln\rho\right) + ... \tag{11}$$

This formulation does not change the time step constrains shown in Equation (8).

Instead by choosing τ_{Spitzer} by hand, we also implemented an auto-adjustment for this quantity. The main idea to choose a reasonable value for τ_{Spitzer} is that we set the time scale of heat diffusion to be the smallest of all relevant time scales in this problem, i.e. the heat diffusion is the fastest process. The next bigger time scale is typically the Alfvén crossing time $\mathrm{d}t_{\mathrm{vA}} = \mathrm{d}x/v_{\mathrm{A}}$ with the Alfvén speed $v_{\mathrm{A}} = B/\sqrt{\mu_0\rho}$. Therefore it make sense to "tie" τ_{Spitzer} to $\mathrm{d}t_{\mathrm{vA}}$ and we set

$$c_{\mathrm{Spitzer}} = \sqrt{2}v_{\mathrm{A}}, \quad \rightarrow \quad \tau_{\mathrm{Spitz}} = \frac{\chi_{\mathrm{Spitzer}}}{2v_{\mathrm{A}}^2}. \tag{12}$$

On one hand we want to avoid τ_{Spitzer} becoming to large and therefore the heat transport less efficient, we choose a upper limit. On the other hand, τ_{Spitzer} would become very small in region below the corona, because there χ_{Spitzer} has very low values because of the low temperature and high density. In this region the heat transport is mainly due to the isotropic heat transport. The low values of τ_{Spitzer} in this regions would cause a very low time step, even though the Spitzer heat flux is not important for the heat transport in this regions. We choose the lower limit to be the advective time step, which assures that τ_{Spitzer} will not affect the time step in these regions.

$$\min\left(\mathrm{d}t_{\mathrm{vA}}, \frac{\mathrm{d}x}{\sqrt{c_{\mathrm{s}}^2 + \boldsymbol{u}^2}}\right) \leq \tau_{\mathrm{Spitzer}} \leq \tau_{\mathrm{Spitz,0}}, \tag{13}$$

where we set $\tau_{\mathrm{Spitz,0}} = 100\,\mathrm{s}$.

To use the non-Fourier heat flux description in the PENCIL CODE, one has to add `HEATFLUX=heatflux` to `src/Makefile.local` and set the parameters in name list `heatflux_run_pars` in `run.in`. The relaxation time τ_{Spitzer} can be either chosen freely and the inverse is set by using `tau_inv_spitzer` or one can switch on the automatically adjustment by using `ltau_spitzer_va=T`, then `tau_inv_spitzer` sets the value of $\tau_{\mathrm{Spitz,0}}$.

2.3. *Semi-relativistic Boris correction*

Above an active region the magnetic field strength can be high and the density low leading to Alfvén speeds comparable to the speed of light (e.g. Chatterjee and Fan 2013, Rempel 2017). This causes two major issues. On one hand the MHD approximation assuming non-relativistic speeds is not valid anymore, i.e. we cannot neglect the displacement current. On the other hand, the high values of the Alfvén speed reduce the time step significantly. To address these two issues we use a semi-relativistic correction of the Lorentz force following the work of Boris (1970) and Gombosi *et al.* (2002), where we apply a semi-relativistic correction term to the Lorentz force. This has been used and successfully tested for the MURAM code in Rempel (2017). Here, we use the implementation discussed by Chatterjee (2018), who added this correction term to the PENCIL CODE. There, the Lorentz force transforms to

$$\frac{\boldsymbol{J} \times \boldsymbol{B}}{\rho} \to \gamma_{\mathrm{A}}^2 \frac{\boldsymbol{J} \times \boldsymbol{B}}{\rho} + \left(1 - \gamma_{\mathrm{A}}^2\right)\left(\boldsymbol{I} - \gamma_{\mathrm{A}}^2 \frac{\boldsymbol{B}\boldsymbol{B}}{\boldsymbol{B}^2}\right)\left(\boldsymbol{u} \cdot \boldsymbol{\nabla}\boldsymbol{u} + \frac{\boldsymbol{\nabla}p}{\rho} - \boldsymbol{g}\right), \tag{14}$$

where $\gamma_{\mathrm{A}}^2 = 1/(1 + v_{\mathrm{A}}^2/c^2)$ is the relativistic correction factor. We note here that the correction term used here and in Chatterjee (2018) is slightly different from the one used by Rempel (2017), because Chatterjee (2018) finds a more accurate way to approximate the inversion of the enhanced inertia matrix. This leads to an additional γ_{A}^2 in front of $\boldsymbol{B}\boldsymbol{B}/\boldsymbol{B}^2$. If $v_{\mathrm{A}} \ll c$ and $\gamma_{\mathrm{A}}^2 \approx 1$ we retain the normal Lorentz force expression. For $v_{\mathrm{A}} \leq c$, the Lorentz force is reduced and the inertia is reduced in the direction perpendicular to the magnetic field. As the enhance inertia matrix (Rempel 2017) is originally on the right hand side of the momentum equation, i.e. under the time derivative and it is just approximated by a correction term on the left hand side, so the semi-relativistic Boris correction does not change the stationary solution of the system and therefore does not lead to further correction terms in the energy equation. To switch on the Boris correction in PENCIL CODE one sets the flag `lboris_correction=T` in the name list `magnetic_run_pars`.

Unlike in Chatterjee (2018), we use the Boris correction also to increase the Alfvén time step, similar to what has been done by Rempel (2017). For this we artificially reduce the speed of light to limit the Alfvén speed $c = c_{\mathrm{A}}$ with the limit c_{A}. As shown by Gombosi *et al.* (2002), the propagation speed can be quite complicated, we choose a similar time step modification

Table 1. Summary of the runs. τ_{Spitzer} is the relaxation time for non-Fourier heat flux description, see Section 2.2, $\tau_{\mathrm{Spitzer}} = \infty$ stands for the use of standard Fourier heat flux, see Equation (4). c_{A} is the Alfvén speed limit, used for the Boris correction, see Section 2.3; $c_{\mathrm{A}} = \infty$ stands for no Boris correction. dt indicates the averaged time step, d$t_{v_{\mathrm{A}}}$ the averaged Alfvén time step and dt_1 and dt_2 the average time step due to the heat flux evolution, see Equation (8). All quantities are determine as an average in the quasi-stationary stage.

Runs	τ_{Spitzer} [ms]	c_{A} [km/s]	dt [ms]	d$t_{v_{\mathrm{A}}}$ [ms]	dt_1[ms]	dt_2 [ms]
R	∞	∞	1.5	2.9	1.7	1.7
H001	10	∞	1.1	2.8	1.2	9.0
H005	50	∞	2.4	2.9	4.4	45.0
H1	1000	∞	4.0	4.6	15.8	900.0
Ha	auto	∞	1.8	2.2	2.2	1.9
B001	10	10 000	1.9	21.2	2.0	9.0
B002	20	10 000	2.3	21.2	2.4	18.0
B005	50	10 000	3.4	21.2	3.7	45.0
B01	100	10 000	2.9	21.2	3.1	90.0
B03	300	10 000	5.4	21.2	6.1	270.0
B1	1000	10 000	8.0	21.2	10.0	900.0
Ba	auto	10 000	15.4	21.2	15.0	19.5
Ba2	auto	3 000	47.6	70.6	49.9	64.9

as in Rempel (2017)

$$\mathrm{d}t_{\mathrm{vA}} \to \mathrm{d}t_{\mathrm{vA}} \sqrt{1 + \left(\frac{v_{\mathrm{A}}^2}{c_{\mathrm{A}}^2}\right)^2} \tag{15}$$

The value can be set by using `va2max_boris` in the name list `magnetic_run_pars`, we choose $c_{\mathrm{A}} = 10\,000\,\mathrm{km/s}$, which corresponds to a time step of $\mathrm{d}t_{\mathrm{vA}} \approx 20\,\mathrm{ms}$ for our simulations.

If the Boris correction is used together with an automatic adjusted relaxing time τ_{Spitzer} in the non-Fourier heat flux calculation, the modification of the Alfvén speed and time step is incorporated in Equations (12) and (13) by setting `va2max_tau_boris` to the same value as `va2max_boris`.

3. Results

We present here the results of three sets of runs, where we used different values of the heat flux relaxation time τ_{Spitzer} in combination with and without the Boris correction. In the first set, containing only Run R, we use the normal treatment of the Spitzer heat flux without using the non-Fourier heat flux evolution and without the Boris correction. In the second set, containing 4 runs (Set H), we use the non-Fourier heat flux evolution with τ_{Spitzer} between $10 - 1000$ ms and the automatically adjustment, see Section 2.2. In the third set, containing 7 runs (Set B), we use the semi-relativistic Boris correction with $c_{\mathrm{A}} = 10\,000\,\mathrm{km/s}$ and non-Fourier heat flux evolution with τ_{Spitzer} between $10 - 1000$ ms and the automatically adjustment. We also use one run with even lower limit for the v_{A} with $c_{\mathrm{A}} = 3\,000\,\mathrm{km/s}$. An overview of the runs can be found in Table 1.

3.1. *Time steps*

As a first step we look at the time steps of all the runs in Table 1. In Run R the averaged time step in the saturated stage is around 1.5 ms. This time step is constrained by the Spitzer time step dt_{Spitzer}. The Alfvén time step dt_{vA} is with 3 ms around twice as large. In the Set H, the code additionally solves the non-Fourier heat flux equation, that leads to increased time steps. Because of the low Alfvén time step, the time step cannot be increased be a large factor. For
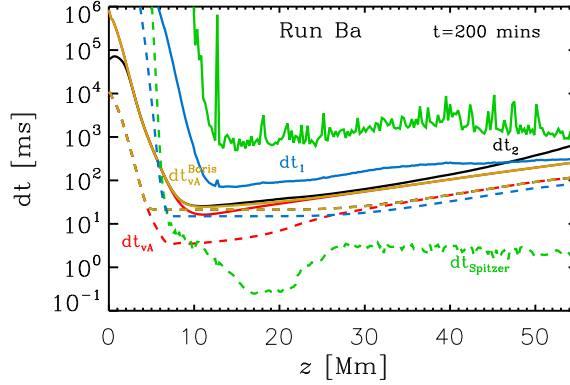
Figure 2.   Vertical distribution of time step constrains for Run Ba at time $t = 200$ mins. We plot the time step due to Spitzer heat conductivity dt_{Spitzer} (green), due to the heat flux dt_1 (black) and dt_2 (blue), due to the Alfvén speed dt_{vA} (red) and reduced Alfvén speed with the Boris correction $dt_{\mathrm{vA}}^{\mathrm{boris}}$. The horizontal averaged values are shown with a solid line and the minimum values at each height with a dashed line.

values of the relaxing time τ_{Spitzer} of 50-1000 ms (Runs H005 and H1), the time step due to the heat flux is much larger than the Alfvén time step. This means that the physical process of heat redistribution is even slower than the Alfvén speed and this can lead to artifacts, as discussed in Section 3.4. For Run H001, the value of τ_{Spitzer} is low enough to have a time step constrain of dt_1 instead of dt_{vA}. However, the runs reach a lower time step than in Run R. In Runs H005 and H1 the time steps are controlled by the Alfvén speed, instead of the heat flux. This leads in Run H1 to higher densities resulting in a lower Alfvén speed and a higher dt_{vA}; see discussions in Section 3.4. When applying the auto-adjustment of τ_{Spitzer}, the time step dt_1 and dt_2 are slightly smaller than dt_{vA} and limits the time step. There, the speed up is less than a factor of two, but the heat distribution is the fastest process in the system. We note here that using the non-Fourier heat flux description leads usually to higher peak temperatures, because the temperature diffusion is less efficient. For the calculation of dt_1 and dt_2, the code uses the CFL pre-factors of 0.9 for both time steps, which results in $dt_2 = 0.9\,\tau_{\mathrm{Spitzer}}$. The time step dt is calculated from the maximum of squared root of the sum of all squared advection speeds, including v_{A} and c_{Spitzer}. Therefore, dt is often lower than dt_1 and dt_{vA}.

To reduce the time step further, we use the semi-relativistic Boris correction in all runs of Set B. As shown in Table 1, dt_{vA} is significantly increased to 21.2 ms for Runs B001-Ba and to 70.6 ms for Ba2. This results in that for Run B001 to Run B1 with $\tau_{\mathrm{Spitzer}} = 10$-1000 ms, dt_1 is lower than dt_{vA} and the time step can be significantly reduced, while the heat distribution is the fastest process in the system. However, we find that using a constant high value for τ_{Spitz} has also its disadvantages. For example, in Run B01, dt does not increase as expected from the other runs of Set B and Set H. The high value of τ_{Spitz} leads in this particular case to larger peak temperature than in the others resulting a decrease of the time step, see discussion in Section 3.3. For Run B1, we achieve a speed up of more than 5, however we need to use a comparable large value of τ_{Spitzer}, which as discussed in Section 3.4 can lead to artifacts. For Runs Ba and Ba2, the auto-adjustment of τ_{Spitzer} takes care that $dt_1 < dt_{\mathrm{vA}}$. We can achieve a speed up of 10 for Run Ba for $c_{\mathrm{A}} = 10\,000\,\mathrm{km/s}$ and of around 30 for Run Ba2 with $c_{\mathrm{A}} = 3\,000\,\mathrm{km/s}$. As discussed below, Run B shows a good agreement with Run R, whereas Run Ba2 tend to produce higher temperatures in the corona.

To get a better understanding of calculation of time step, we plot in the Fig. 2 the various contribution to the time steps for Run Ba. Without the non-Fourier heat flux description and the Boris correction, the time step is dominated by Alfvén time step dt_{vA} and the Spitzer time step dt_{Spitzer}. The Boris correction reduces dt_{vA} to $dt_{\mathrm{vA}}^{\mathrm{Boris}}$ mostly in the regions 5 and 30 Mm. The auto-adjustment of τ_{Spitzer} sets dt_1 to be always slightly lower than the $dt_{\mathrm{vA}}^{\mathrm{Boris}}$. Only below $z = 5\,\mathrm{Mm}$, $dt_{\mathrm{vA}}^{\mathrm{Boris}}$ is small, because there the temperature diffusion is dominated
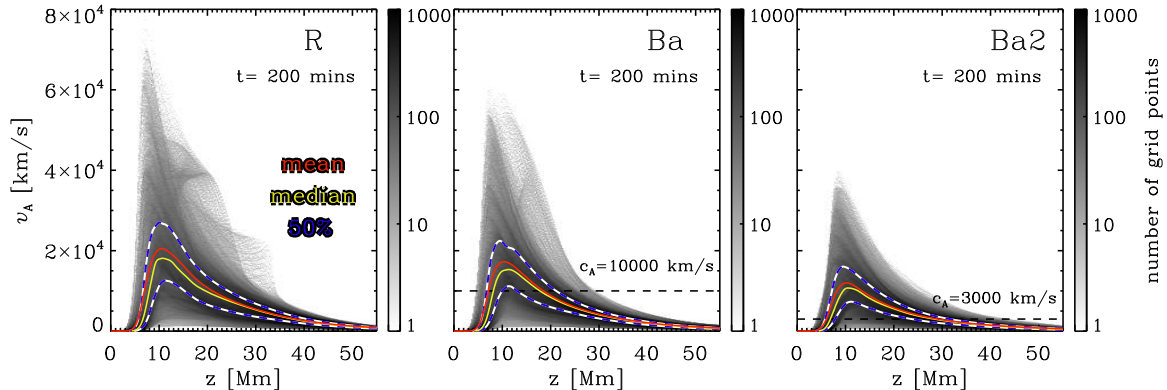
Figure 3. 2D histogram of the Alfvén speed over height z for Runs R, Ba, Ba2. We plot with the mean value (red solid line), median (yellow solid). The dashed white-blue lines show the 25 and 75 percentiles, i.e. half of the data points are in between these lines. The black dashed line indicate the Alfvén speed limit c_A for the Boris correction.

by other heat diffusion mechanism. It is clearly visible that the dt_1 is significantly higher than $dt_{Spitzer}$ (green line) and dt_{vA} (red) without the Boris correction. However, we note here that the because of the non-Fourier heat flux description we find higher peak temperatures in the simulation. This results in a decrease of $dt_{Spitzer}$ in comparison with runs without the non-Fourier heat flux description. In Run R, dt_{Spitz} is around 1.6 ms, where in Run Ba, it is much lower.

3.2.   *Alfvén velocity with Boris correction*

Next, we look at the influence of the semi-relativistic Boris correction on the Alfvén velocity v_A. In Fig. 3, we plot 2D histogram of v_A for Runs R, Ba, Ba2. For Run R, the maximum speed reaches $v_A = 80\,000$ km/s at the lower part of the corona, where the density has already dropped significantly, but the magnetic field is still strong. The median (yellow line) has it maximum at the same location with a value around $v_A = 18\,000$ km/s. In Run Ba, we have applied the Boris correction with $c_A = 10\,000$ km/s. Even though, this value is lower than the averaged and mean value in the region of $z = 5$–20 Mm, the velocity distribution does not change significantly in comparison to Run R. As a main effect of the Boris correction, the peak velocity at the top of the distribution is reduced, therefore the distribution becomes more compact. This can be also seen from the seen from the changes in the mean and median velocity. While the maximum of the mean is reduced from above $v_A = 20\,000$ km/s of Run R to nearly $v_A = 15\,000$ km/s, changes the meridian just slightly. Also, the velocities, where 50% of the points are located reduced only slightly. This make us confident that the Boris correction with $c_A = 10\,000$ km/s does only reduces the peak velocities and not the overall velocity structure; most of the points are unaffected by the correction.

For Run Ba2, we reduce the Alfvén speed limit to $c_A = 3\,000$ km/s. This makes the velocity distribution even more compact. The maximum values are significantly reduced to $v_A = 35\,000$ km/s, and the mean and median values are also lower than in Runs R, Ba. However, setting $c_A = 3\,000$ km/s does not mean that all the velocities are lower than this value, it can more understandable to reduce the peak velocity significantly and transfer the distribution to a much more compact form.

3.3.   *Structure of temperature and ohmic heating*

Next, we look at the averaged temperature profile over height. Even though the non-Fourier description of the heat flux can lead to higher peak temperatures, the overall temperature
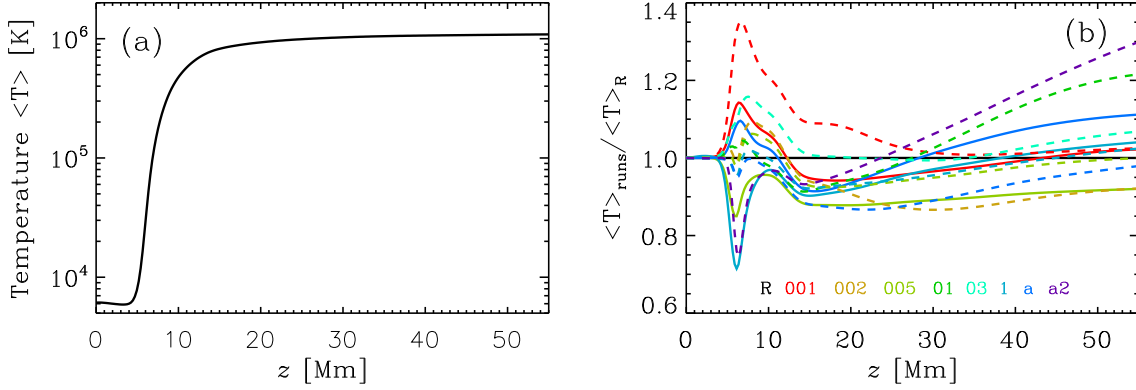
Figure 4.   (a) Averaged temperature $\langle T \rangle$ as a function of height z for Run R. (b) Ratio of the averaged temperature profile of all runs and Run R $\langle T \rangle_{\rm runs}/\langle T \rangle_R$ as a function of height z. The temperatures are averaged horizontal as well as in time for the last quarter (1 hours) of the simulation. The color of the lines indicates the run names in terms of $\tau_{\rm Spitzer}$, the solid lines are for runs of Sets R and H, and dashed lines for Set B.
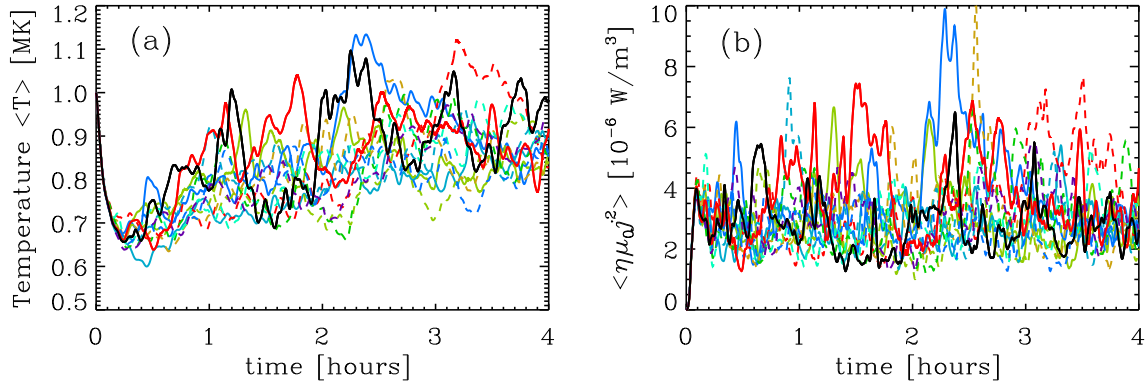
Figure 5.   Time evolution of the horizontal averaged temperature $\langle T \rangle$ (a) and of the horizontal averaged heating rate $\langle \mu_0 \eta \boldsymbol{j}^2 \rangle$ (b) at $z = 18 - 22 \, {\rm Mm}$. Color coding is the same as in Fig. 4.

structure should remain roughly the same. In Fig. 4, we plot the horizontal averaged temperature profile over height for the reference Run R in panel a and a comparison with the other runs in panel b. The horizontal averaged temperature structure in Run R shows a typical behavior of corona above an active region with medium magnetic field strengths. The temperature above $z = 10$ Mm is heated self-consistently to averaged values of around 1 Million Kelvin. This temperature profile is very similar to results of earlier work with the Pencil Code (e.g. Bingert 2009, Bingert and Peter 2011, 2013, Bourdin *et al.* 2013) and other groups (e.g. Gudiksen and Nordlund 2002, 2005b,a, Gudiksen *et al.* 2011). When comparing with the temperature profiles of the other runs, we find no large differences. For most of the runs the deviation is not more than 10%. For some runs the largest difference occur in the transition region, where the temperature has a large gradient. Higher temperatures in this region simply means that the transition region is starts slightly at lower heights and smaller values means a slightly higher transition region. Runs H001, Ha, B001, B002, B01, B03 seems to develop a lower transition region, whereas Runs H005, H1, B005, B1, Ba, Ba2 develop a higher transition region. Only Runs B01 and Ba2 heat the corona to 20% to 30% higher temperature in upper corona in comparison with Run R. In these runs, the heat diffusion might be not efficient enough to transport the heat to lower layers. When we look at the temperature evolution over time, as plotted in Fig. 5a, we also find no large differences between the runs. The main differences occur because of temporal variations of the temperature in each run.

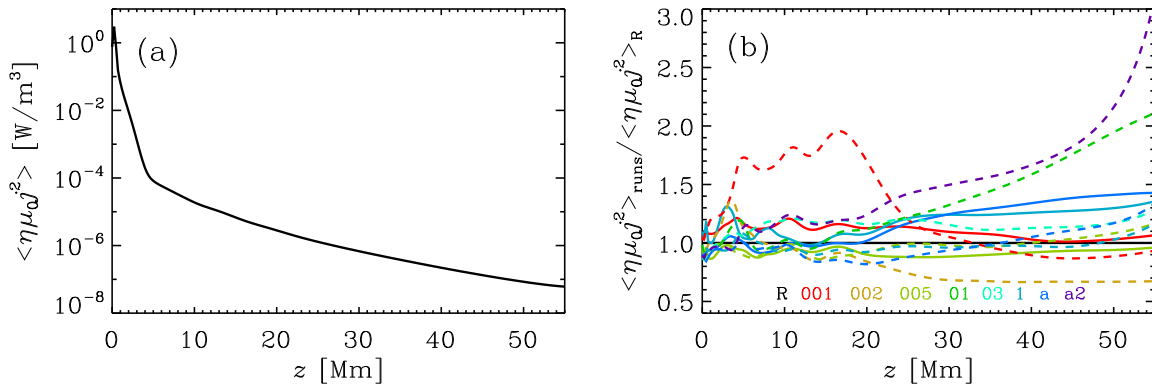Next, we look at the ohmic heating rate in all the runs. The ohmic heating is the main

Figure 6. (a) Averaged ohmic heating rate $\langle\mu_0\eta j^2\rangle$ as a function of height z for Run R. (b) Ratio of the averaged ohmic heating rate of all runs and Run R $\langle T\rangle_{\text{runs}}/\langle T\rangle_R$ as a function of height z. The ohmic heating rate are averaged horizontal as well as in time for the last quarter (1 hours) of the simulation. The color coding the same as in Figs. 4 and 5.

heating process in this type of simulations to heat the coronal plasma up to millions of Kelvin. Also, here, we plot the horizontal averaged profile of Run R in panel a of Fig. 6 and compare it with the other runs in Fig. 6b. The profile of the ohmic heating rate shows the typical behavior of an exponential decrease corresponding to two scale heights. Below the corona the scale height is roughly 0.5 Mm, while in the corona the scale height is around 5 Mm. Also, this is consistent with earlier finding with this kind of simulations by many groups. By comparing with the other runs, we find that these agree well with Run R. Run B001 shows also in the heating rate signatures of a lower transition region. Runs B01 and Ba2 develop a higher heating in the upper corona resulting in the higher temperature, we found in Fig. 4. Small changes either in the scale height of the coronal heating or in the location in the transition region can explain most of the differences we find in the comparison with Run R. This explains also the temporal changes of the heating rate at constant height, as shown in Fig. 5b. Overall, the vertical horizontal average temperature and heating structure of all runs agrees well with Run R.

3.4. *Emission signatures*

To further test how well the non-Fourier description of the heat flux reproduce the Fourier description, we synthesize coronal emissivities corresponding to the 171 Å channel of Atmospheric Imaging Assembly (AIA; Boerner *et al.* 2012) on board of SDO. For this we calculate the emission following optical thin radiation approximation.

$$\epsilon = n_e^2 G(T), \tag{16}$$

where $G(T)$ is the response function of the particular filter, we want to to synthesize. Because we compare here our simulations among each other and not to observation, we simplify $G(T)$ using a gaussian distribution around a mean temperature $\log_{10} T_0$.

$$G(T) \propto \exp\left[-\left(\frac{\log_{10} T - \log_{10} T_0}{\Delta\log_{10} T_0}\right)^2\right], \tag{17}$$

where $\Delta\log_{10} T_0$ are the temperature width, used to mimic the temperature response function. We use $\log_{10} T_0 = 6 \log_{10}$ K and $\Delta\log_{10} T_0 = 0.2 \log_{10}$ K for synthesizing the emission of the AIA 171Å channel.

In Fig. 7, we plot a temperature xz-cut at $y = 50\,\text{Mm}$ together with the synthesized emission representing the AIA 171 channel for Run R, Ha, Ba, Ba2. For these runs, we expect a
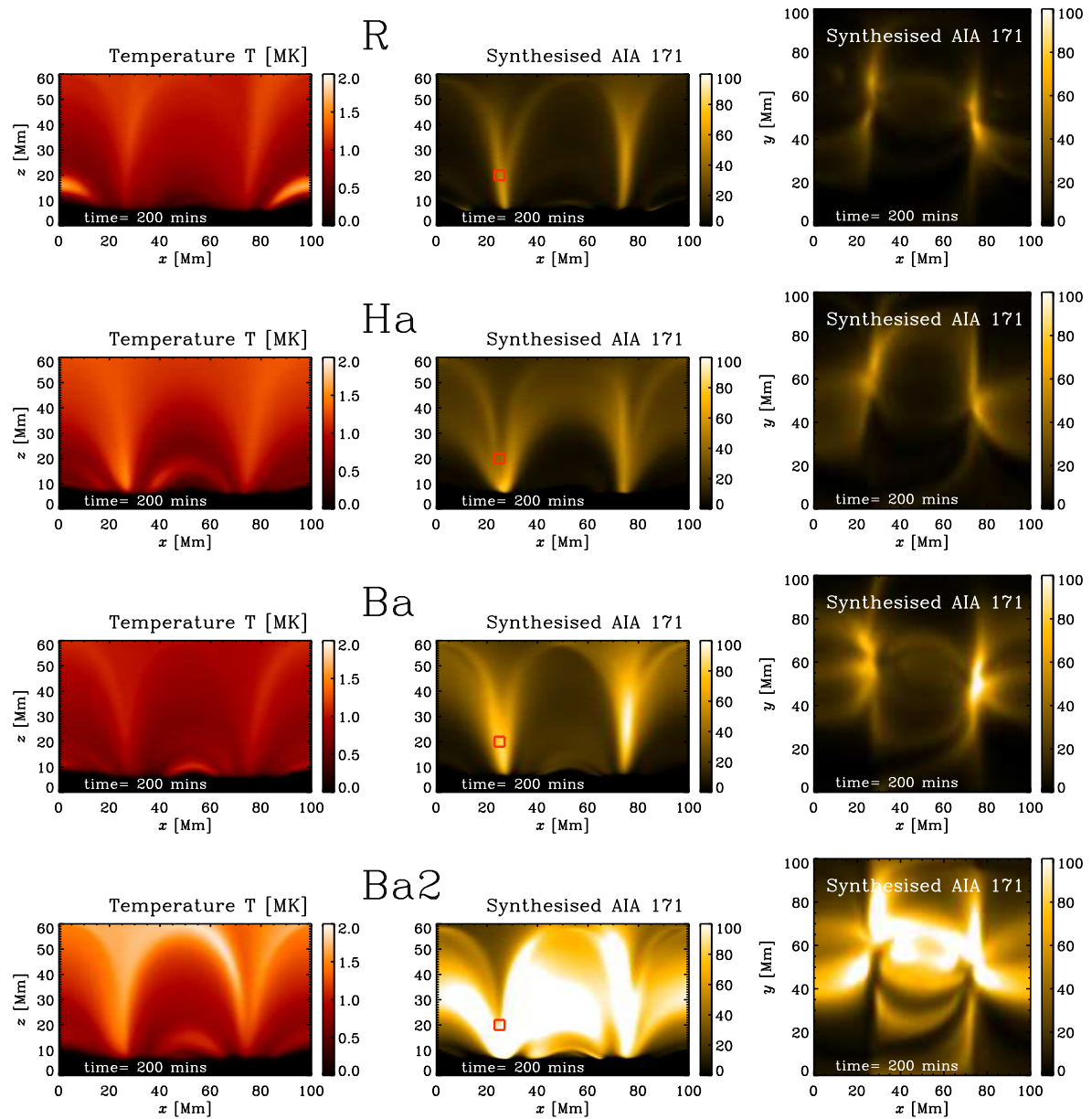
Figure 7. Temperature and emission structure for Runs R, Ha, Ba, Ba2. We show a temperature cut at $y = 50$ Mm (left panel) and the to synthesized emission comparable to the AIA 171 channel, representing emission at around 1 MK, integrated in the y direction (side view, middle panel) and in z direction (top view, right panel). The emission values represent the count rate of the AIA instrument. The red square indicate the region which is used to calculate the temporal evolution in Fig. 8.

good agreement between Run R and Run Ha, Ba, Ba2, because the value of τ_{Spitzer} is regulated automatic and therefore the time step is controlled by the heat flux dt_1. There is some agreement between the Run R, Ha and Ba, but we find slightly stronger emission structures for Run Ba. However, we have to take into account that the emission is calculated from a single snapshot at $t = 200$ min for every run. So, small variation are expected to occur over time, which can explain the visual difference between Run R and Run Ba. To illustrate this we show in Fig. 8 the time evolution of emission in a small region of the simulation box. We find good agreement for Runs R and Ha, where the temporal variation in the saturated stage (after 150 mins) are big enough to explain the differences seen in Fig. 7. Run Ba takes a bit
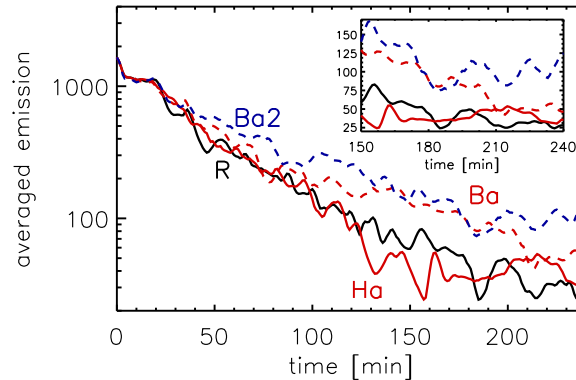
Figure 8. Time evolution of emission averaged over a small region for Run R, Ha, Ba and Ba2. We plot the emission of the AIA 171 channel in the y direction averaged over a small region ($x = 23 - 27 Mm, z = 1822 Mm$) as indicated by red boxes in Fig. 7 middle panels. The inlay shows the time evolution of the averaged emission from 150 to 240 mins on a linear scale instead of logarithmic. The color and style of the lines are the same as in Fig. 4

longer to saturate, but at around 220 mins it also settles to values similar to Runs R and Ha. Run Ba2 seems to saturate to a much higher emission level than the other runs, which is already seen in Fig. 7.

For Run Ba2, as pointed out in Section 3.3, the corona is heated to higher temperatures, i.e. the heat transport is less efficient. We find larger temperatures mostly at the top of the corona inside the loop structures. This leads also to higher emission in the AIA 171 channel, which is much higher than in the Run R. This might be an artifact from the low limit of the Alfvén speed through the Boris correction in this run.

In Fig. 9, we show a few other runs, which either dominated by the Alfvén time step (Runs H005 and H1) or use a constant value of τ_{Spitzer} (Runs B03 and B1). Run H005 shows a similar emission structure than the Runs R, Ha, Ba, however the emission is slightly larger in the legs of the loop. As also here the temperatures are not significantly higher, the difference is due to the slightly higher density in these regions. For Run H1, the fact that the τ_{Spitzer} is large and the time step controlled by the Alfvén time lead to larger temperatures and therefore higher emission. However, also here the density in the corona loops is larger than in Run R, leading not only to higher emission, but also to a smaller Alfvén time step, see Table 1. The time step in Runs B03 and B1 are controlled by the time step of the heat flux $\mathrm{d}t_1$. There, as expected, we see similar emission loop structures as in Run R, Ha and Ba. They are slightly larger in Run B1 than in Run B03. This means that simulations using either the automatic adjustment or a constant value of τ_{Spitzer} reproduce well the emission structure of Run R, as long as the time step is still controlled by the heat flux time step $\mathrm{d}t_1$, however the emission tend to be slightly larger. There are a few exceptions: for too low values of the Alfvén limiter the emission and temperature become much larger. For simulation, where the time step is controlled by Alfvén time step, but use small values of τ_{Spitzer}, the emission structure can be also reproduced.

4. Discussion and conclusions

In this work we present the new implementation of a non-Fourier description of the heat flux to PENCIL CODE. We discuss the advantages and the limitations using the example of 3D MHD simulations of the solar corona. The implementation of the auto-adjustment of τ_{Spitzer} is slightly different from the implementation used in Rempel (2017) in the sense that we ensure the heat flux time step to be always by square root of two smaller than the Alfvén time step, whereas in Rempel (2017) they are chosen to be the same. Even though a detailed comparison
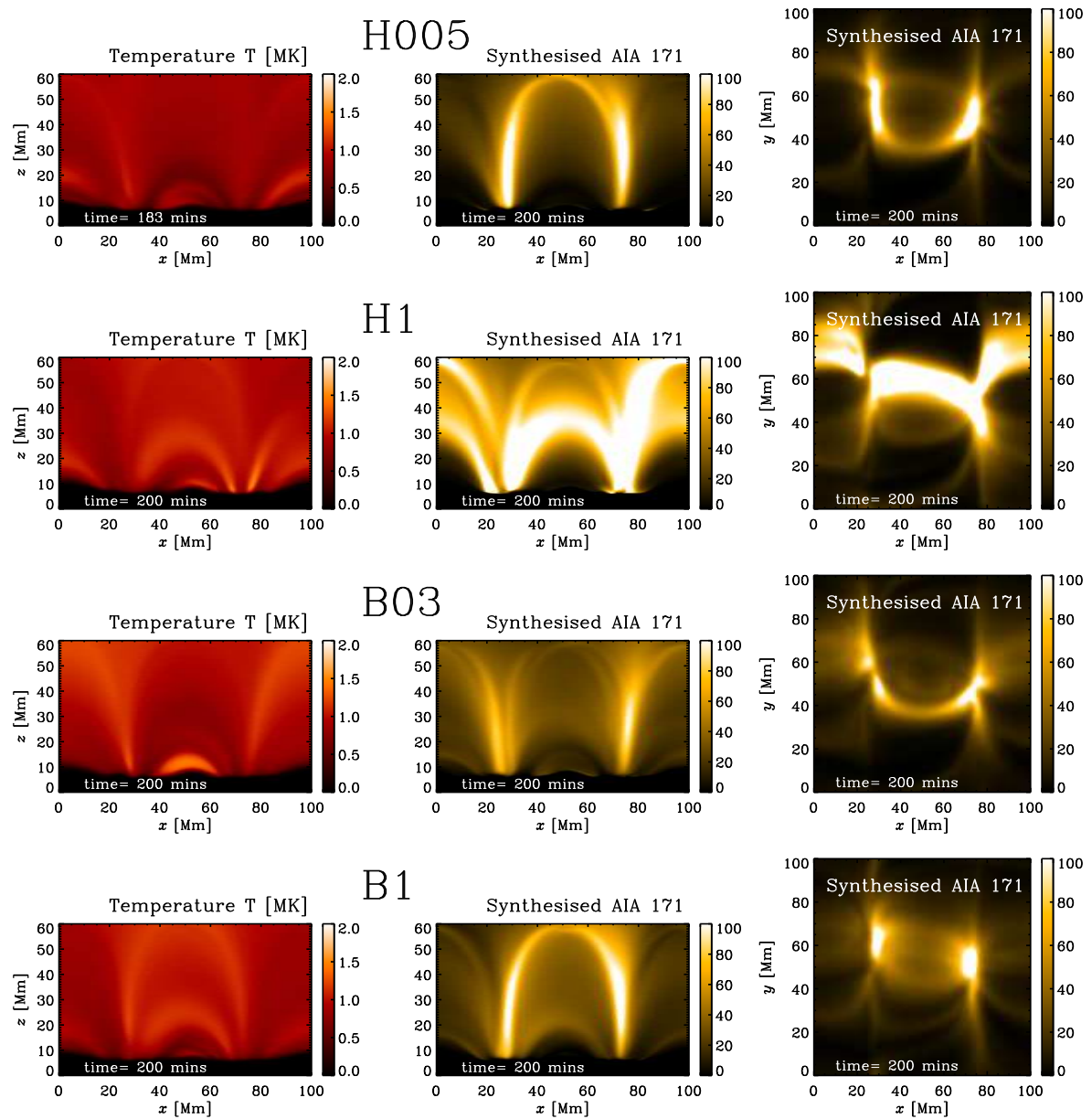
Figure 9.   Temperature and emission structure for Runs H005, H1, B03, B1. We show a temperature xz-cut at $y = 50$ Mm (left panel) and the to synthesized emission comparable to the AIA 171 channel representing emission at around 1 MK, integrated in the y direction (side view, middle panel) and in z direction (top view, right panel). The emission values represent the count rate of the AIA instrument. These runs are expected to give a rather bad agreement with the reference Run R.

was not conducted here, we see indications that our choice leads to a better stability of the simulations. We find that using the non-Fourier description of the heat flux alone allows for a small speed up, because in our case the time constrain of the Alfvén speed is large. For simulations with a lower magnetic field strength, we would expect a larger speed up. If we choose τ_{Spitzer} to be a constant, so that the heat flux time step is four times higher than the Alfvén time step, the temperatures and the emission are significant larger than in the other runs. This seems to be an artifact of this choice.

We further test the implementation of the semi-relativistic Boris correction (Boris 1970) as a limit for the Alfvén speed. The implementation to the PENCIL CODE is slightly different from

the one used by Rempel (2017) and Gombosi *et al.* (2002), see Chatterjee (2018) for details. The Boris correction does not limit the Alfvén speed at all locations to the limit chosen, it actually reduces the peak velocities, which are not very abundant. Therefore, this correction makes the velocity distribution much more compact. The lower the limit, the more compact is the velocity distribution. Using the Boris correction allows for a significant speed up of around ten. For higher speed up, i.e., lower limit for Alfvén speed, the simulation develops higher temperatures and emission signatures than the reference run. The auto-adjustment together with Boris correction works very well to reproduce the temperatures and emission structures of the reference run with a speed up of around ten. These results convince us that we use the non-Fourier heat flux description together with the Boris correction to acquire a significant speed up of the simulation without losing a correct representation of the physical processes within the solar corona.

In the future, we are planning to use these implementations to perform large-scale active region simulations similar as done by Bourdin *et al.* (2013, 2014), which can be then run for a much longer time and allowing the study of hot core loop formations. Furthermore, this implementation allows us to perform parameter studies to investigate the coronal response to different kinds of active regions on the Sun, but also on other stars. Finally, through these improvements, we get closer to the possibility to simulated a more realistic convection-zone-corona model as started in Warnecke *et al.* (2012b, 2013a, 2016a).

Acknowledgements

References

Abbett, W.P., The Magnetic Connection between the Convection Zone and Corona in the Quiet Sun. *ApJ*, 2007, **665**, 1469–1488.

Bingert, S. and Peter, H., Intermittent heating in the solar corona employing a 3D MHD model. *A&A*, 2011, **530**, A112.

Bingert, S. and Peter, H., Nanoflare statistics in an active region 3D MHD coronal model. *A&A*, 2013, **550**, A30.

Bingert, S., 3D MHD models of the solar corona: active region and network. Ph.D. Thesis, Albert-Ludwig-Universität Freiburg, 2009.

Boerner, P., Edwards, C., Lemen, J., Rausch, A., Schrijver, C., Shine, R., Shing, L., Stern, R., Tarbell, T., Title, A., Wolfson, C.J., Soufli, R., Spiller, E., Gullikson, E., McKenzie, D., Windt, D., Golub, L., Podgorski, W., Testa, P. and Weber, M., Initial Calibration of the Atmospheric Imaging Assembly (AIA) on the Solar Dynamics Observatory (SDO). *Sol. Phys.*, 2012, **275**, 41–66.

Boris, J.P., A physically Motivated Solution of the Alfven. Problem. *NRL Memorandum Report*, 1970, **2167**.

Bourdin, P.A., Bingert, S. and Peter, H., Observationally driven 3D magnetohydrodynamics model of the solar corona above an active region. *A&A*, 2013, **555**, A123.

Bourdin, P.A., Bingert, S. and Peter, H., Coronal loops above an active region: Observation versus model. *PASJ*, 2014, **66**, S7.

Brandenburg, A. and Chatterjee, P., Strong nonlocality variations in a spherical mean-field dynamo. *Astronomische Nachrichten*, 2018, **339**, 118–126.

Brandenburg, A., Käpylä, P.J. and Mohammed, A., Non-Fickian diffusion and tau approximation from numerical turbulence. *Physics of Fluids*, 2004, **16**, 1020–1027.

Chatterjee, P., Testing Alfv\'en wave propagation in a realistic set-up of the solar atmosphere. *Geophys. Astrophys. Fluid Dyn., submitted, arXiv: 1806.08166*, 2018.

Chatterjee, P. and Fan, Y., Simulation of Homologous and Cannibalistic Coronal Mass Ejections produced by the Emergence of a Twisted Flux Rope into the Solar Corona. *ApJ*, 2013, **778**, L8.

Chen, F., Peter, H., Bingert, S. and Cheung, M.C.M., A model for the formation of the active region corona driven by magnetic flux emergence. *A&A*, 2014, **564**, A12.

Chen, F., Peter, H., Bingert, S. and Cheung, M.C.M., Magnetic jam in the corona of the Sun. *Nat Phys*, 2015, **11**, 492–495.

Cook, J.W., Cheng, C.C., Jacobs, V.L. and Antiochos, S.K., Effect of coronal elemental abundances on the radiative loss function. *ApJ*, 1989, **338**, 1176–1183.

Galsgaard, K. and Nordlund, Å., Heating and activity of the solar corona 1. Boundary shearing of an initially homogeneous magnetic field. *J. Geophys. Res.*, 1996, **101**, 13445–13460.

Gent, F.A., Shukurov, A., Fletcher, A., Sarson, G.R. and Mantere, M.J., The supernova-regulated ISM - I. The multiphase structure. *MNRAS*, 2013, **432**, 1396–1423.

Gombosi, T.I., Tóth, G., De Zeeuw, D.L., Hansen, K.C., Kabin, K. and Powell, K.G., Semirelativistic Magnetohydrodynamics and Physics-Based Convergence Acceleration. *Journal of Computational Physics*, 2002, **177**, 176–205.

Gudiksen, B.V., Carlsson, M., Hansteen, V.H., Hayek, W., Leenaarts, J. and Martínez-Sykora, J., The stellar atmosphere simulation code Bifrost. Code description and validation. *A&A*, 2011, **531**, A154.

Gudiksen, B.V. and Nordlund, Å., Bulk Heating and Slender Magnetic Loops in the Solar Corona. *ApJ*, 2002, **572**, L113–L116.

Gudiksen, B.V. and Nordlund, Å., An Ab Initio Approach to Solar Coronal Loops. *ApJ*, 2005a, **618**, 1031–1038.

Gudiksen, B.V. and Nordlund, Å., An Ab Initio Approach to the Solar Coronal Heating Problem. *ApJ*, 2005b, **618**, 1020–1030.

Hansteen, V.H., Hara, H., De Pontieu, B. and Carlsson, M., On Redshifts and Blueshifts in the Transition Region and Corona. *ApJ*, 2010, **718**, 1070–1078.

Haugen, N.E.L., Brandenburg, A. and Mee, A.J., Mach number dependence of the onset of dynamo action. *MNRAS*, 2004, **353**, 947–952.

Hubbard, A. and Brandenburg, A., Memory Effects in Turbulent Transport. *ApJ*, 2009, **706**, 712–726.

Losada, I.R., Warnecke, J., Brandenburg, A., Kleeorin, N. and Rogachevskii, I., Magnetic bipoles in rotating turbulence with coronal envelope. *A&A, in press, (arXiv:1803.04446)*, 2018.

Mok, Y., Mikić, Z., Lionello, R. and Linker, J.A., Calculating the Thermal Structure of Solar Active Regions in Three Dimensions. *ApJ*, 2005, **621**, 1098–1108.

Mok, Y., Mikić, Z., Lionello, R. and Linker, J.A., The Formation of Coronal Loops by Thermal Instability in Three Dimensions. *ApJ*, 2008, **679**, L161.

Parker, E.N., Topological Dissipation and the Small-Scale Fields in Turbulent Gases. *ApJ*, 1972, **174**, 499.

Parker, E.N., Nanoflares and the solar X-ray corona. *ApJ*, 1988, **330**, 474–479.

Peter, H., What can large-scale magnetohydrodynamic numerical experiments tell us about coronal heating?. *Philosophical Transactions of the Royal Society of London Series A*, 2015, **373**, 20150055–20150055.

Peter, H., Gudiksen, B.V. and Nordlund, Å., Coronal Heating through Braiding of Magnetic Field Lines. *ApJ*, 2004, **617**, L85–L88.

Peter, H., Gudiksen, B.V. and Nordlund, Å., Forward Modeling of the Corona of the Sun and Solar-like Stars: From a Three-dimensional Magnetohydrodynamic Model to Synthetic Extreme-Ultraviolet Spectra. *ApJ*, 2006, **638**, 1086–1100.

Peter, H., Warnecke, J., Chitta, L.P. and Cameron, R.H., Limitations of force-free magnetic field extrapolations: Revisiting basic assumptions. *A&A*, 2015, **584**, A68.

Rempel, M., Numerical Simulations of Quiet Sun Magnetism: On the Contribution from a Small-scale Dynamo. *ApJ*, 2014, **789**, 132.

Rempel, M., Extension of the MURaM Radiative MHD Code for Coronal Simulations. *ApJ*, 2017, **834**, 10.

Rheinhardt, M. and Brandenburg, A., Modeling spatio-temporal nonlocality in mean-field dynamos. *Astron. Nachr.*, 2012, **333**, 71–77.

Schou, J., Scherrer, P.H., Bush, R.I., Wachter, R., Couvidat, S., Rabello-Soares, M.C., Bogart, R.S., Hoeksema, J.T., Liu, Y., Duvall, T.L., Akin, D.J., Allard, B.A., Miles, J.W., Rairden, R., Shine, R.A., Tarbell, T.D., Title, A.M., Wolfson, C.J., Elmore, D.F., Norton, A.A. and Tomczyk, S., Design and Ground Calibration of the Helioseismic and Magnetic Imager (HMI) Instrument on the Solar Dynamics Observatory (SDO). *Sol. Phys.*, 2012, **275**, 229–259.

van der Holst, B., Sokolov, I.V., Meng, X., Jin, M., Manchester, IV, W.B., Tóth, G. and Gombosi, T.I., Alfvén Wave Solar Model (AWSoM): Coronal Heating. *ApJ*, 2014, **782**, 81.

Vögler, A., Shelyag, S., Schüssler, M., Cattaneo, F., Emonet, T. and Linde, T., Simulations of magnetoconvection in the solar photosphere. Equations, methods, and results of the MURaM code. *A&A*, 2005, **429**, 335–351.

Warnecke, J. and Brandenburg, A., Surface appearance of dynamo-generated large-scale fields. *A&A*, 2010, **523**, A19.

Warnecke, J. and Brandenburg, A., Coronal influence on dynamos; in *IAU Symposium*, Vol. 302 of *IAU Symposium*, Aug., 2014, pp. 134–137.

Warnecke, J., Brandenburg, A. and Mitra, D., Dynamo-driven plasmoid ejections above a spherical surface. *A&A*, 2011, **534**, A11.

Warnecke, J., Brandenburg, A. and Mitra, D., Magnetic twist: a source and property of space weather. *JSWSC*, 2012a, **2**, A11.

Warnecke, J., Chen, F., Bingert, S. and Peter, H., Current systems of coronal loops in 3D MHD simulations. *A&A*, 2017, **607**, A53.

Warnecke, J., Käpylä, P.J., Käpylä, M.J. and Brandenburg, A., Influence of a coronal envelope as a free boundary to global convective dynamo simulations. *A&A*, 2016a, **596**, A115.

Warnecke, J., Käpylä, P.J., Mantere, M.J. and Brandenburg, A., Ejections of Magnetic Structures Above a Spherical Wedge Driven by a Convective Dynamo with Differential Rotation. *Sol. Phys.*, 2012b, **280**, 299–319.

Warnecke, J., Käpylä, P.J., Mantere, M.J. and Brandenburg, A., Spoke-like Differential Rotation in a Convective Dynamo with a Coronal Envelope. *ApJ*, 2013a, **778**, 141.

Warnecke, J., Losada, I.R., Brandenburg, A., Kleeorin, N. and Rogachevskii, I., Bipolar Magnetic Structures Driven by Stratified Turbulence with a Coronal Envelope. *ApJ*, 2013b, **777**, L37.

Warnecke, J., Losada, I.R., Brandenburg, A., Kleeorin, N. and Rogachevskii, I., Bipolar region formation in stratified two-layer turbulence. *A&A*, 2016b, **589**, A125.

Wiegelmann, T., Nonlinear force-free modeling of the solar coronal magnetic field. *J. Geophys. Res.*, 2008, **113**, A12.